APPLICATIONS OF MRI IN FLUIDICS:

SINGLE ECHO ACQUISITION MRI TOWARD MICROFLUIDICS

A Senior Honors Thesis

by

JOHN CARL BOSSHARD

Submitted to the Office of Honors Programs
& Academic Scholarships
Texas A&M University
In partial fulfillment of the requirements of the

UNIVERSITY UNDERGRADUATE
RESEARCH FELLOWS

April 2006

Major: Electrical Engineering

APPLICATIONS OF MRI IN FLUIDICS:

SINGLE ECHO ACQUISITION MRI TOWARD MICROFLUIDICS

A Senior Honors Thesis

by

JOHN CARL BOSSHARD

Submitted to the Office of Honors Programs
& Academic Scholarships
Texas A&M University
In partial fulfillment for the designation of

UNIVERSITY UNDERGRADUATE
RESEARCH FELLOWS

Approved as to style and content by:

-------------------------------------   --------------------------------------
Steven M. Wright   Edward A. Funkhouser
(Fellows Advisor)   (Executive Director)

April 2006

Major: Electrical Engineering

ABSTRACT

Applications of MRI in Fluidics:

Single Echo Acquisition MRI Toward Microfluidics (April 2006)

John C. Bosshard
Department of Electrical Engineering
Texas A&M University

Fellows Advisor: Dr. Steven M. Wright
Department of Electrical Engineering

Microscale devices capable of manipulating fluids have potential to give rise to a

paradigm shift in the fields of biology and medicine. The purpose of this research is to

assess the feasibility of applying single echo acquisition (SEA) magnetic resonance

imaging (MRI) to microscale fluid flow quantification. This is important because

development and improvement of microfluidic devices requires the ability to accurately

and non-invasively measure microscale flow. Lab-on-a-chip aims to integrate an array

of chemical laboratory tools onto a single chip, utilizing microfluidic flow for mass

transport. Use of microfluidics results in improved speed and efficiency and allows

operations that harness physical properties unique to the microscale. Current microscale

flow visualization methods rely on fluorescence, requiring optically non-opaque fluids and device boundaries. Furthermore, these methods require insertion of labeled chemicals or seed particles into the flow, which may interfere with processes under observation. MRI has an established history of non-invasively quantifying flow through opaque boundaries but is limited by its slow image acquisition rate. SEA employs a 64-channel array coil to acquire a full image with each echo, significantly improving temporal resolution. Methods involve assessing the performance of SEA flow velocimetry on a scale of several millimeters by utilizing time-of-flight techniques. By taking a series of 5 ms snapshots, quantitative velocity information is obtained for laminar, transitional, and turbulent flow with Reynolds numbers ranging from 100 to 1200. Findings show that the turbulent eddies are visible and velocity information can be extracted from images, which means that SEA can accurately asses flow at the millimeter scale. In addition, SEA allows visualization of turbulent flow not accessible to standard MRI velocimetry techniques. It is concluded that SEA could be adapted as new tool for non-invasive quantification of optically inaccessible flow. Implications of this are that through integrated radio frequency microcoils, SEA MRI could be adapted as a new tool to study microfluidic flow resulting in improved microfluidic devices.

ACKNOWLEDGEMENTS

TABLE OF CONTENTS

LIST OF FIGURES

LIST OF TABLES

I. INTRODUCTION[1]

The ability to visualize microfluidic flow is of paramount importance to the

development of new microfluidic devices. As indicated by the literature, leading

visualization methods have several disadvantages.   The purpose of this work is to assess

the feasibility of extending Single Echo Acquisition (SEA) Magnetic Resonance

Imaging (MRI) to microscale fluid flow visualization. Better microfluidic flow

visualization would benefit the creation of new microfluidic devices and lab-on-a-chip

systems. Such devices could impact biology and medicine, and have the potential to

improve the quality of life of many. It is expected that by demonstrating SEA MRI's

ability to study macroscale flow, its utility at the microscale will be established.

Significant findings are that SEA is able to visualize flow in a separation channel at up

to 200 frames per second, showing complex phenomena such as mixing and rotation.

Lab-on-a-chip

Lab-on-a-chip, also called a micro total analysis system (μTAS), is a developing

technology that seeks to integrate many of the tools employed in analytical chemistry

onto a single chip. While this concept is not new, the tools to miniaturize analytical

---

[1] This thesis follows the style and format of *Magnetic Resonance in Medicine.*

systems have only become available with advances in integrated circuit production techniques, such as photolithography (1). The initial concept of μTAS states that it is capable of performing all sample handling extremely close to the place of measurement and includes provisions for sample pretreatment, separation, and detection (2). Advantages include greater speed and efficiency, reduced consumption of reagents, and capability of multiple simultaneous measurements. Also, human error and contamination are reduced by eliminating the need for many manual manipulations (1). Several lab-on-a-chip systems have been realized and many of the microfluidic devices to be implemented in a lab-on-a-chip have undergone extensive research and development by both academia and industry. Further improvement of these devices is a critical step in forming a fully integrated device.

Lab-on-a-chip holds the potential to dramatically change the way biology and medicine are performed. One application of lab-on-a-chip is in point-of-care testing in clinical chemistry (3). By creating small, fast, and easy to operate devices, healthcare testing could be moved from central laboratories and into the doctor's office. This offers a number of advantages. Highly complex tests can be performed by relatively unskilled workers through the integration of multiple steps of procedures within one lightweight

portable device (4). The need to maintain sophisticated laboratories of costly equipment

and skilled technicians to perform tests would be eliminated (1). While this reduces the

cost of performing tests, a chemical analysis performed on-chip is also less expensive

due to decreased reagent consumption and analysis time. No longer would a separate

visit to the hospital be necessary to provide a sample for laboratory analysis. Rather,

during a visit with the physician a single drop of blood could be analyzed on the spot.

This could result in quick and efficient disease diagnosis and treatment monitoring.

With increasing understanding of genetic information, physicians will become

more reliant on molecular diagnostics, which use DNA or RNA along with molecular

genetics to perform diagnostic testing on patients (5). Lab-on-a-chip may be applied to

replace current labor-intensive molecular diagnostic technologies, facilitating detection

of genetic diseases. Many of these devices will likely be manufactured at little expense

and thus will be disposable, eliminating any carry-over in analysis. There are also

applications in intensive care units, such as monitoring of cardiac markers (3). By

detecting an abnormal presence or absence of several cardiac proteins, or cardiac

markers, better emergency room diagnosis may be possible for patients with chest pain,

such as detection of acute myocardial infarction (6). Point-of-care testing could enable

fast diagnostic monitoring in close proximity to the patient as in operating rooms, aiding in decision-making. Finally, patients could monitor themselves daily at home.

Through speed, automation, and parallel operation, lab-on-a-chip could revolutionize drug discovery. Combinational chemistry generates many drug candidates by liking several chemical building blocks in all possible combinations (7). This demands simultaneous, rapid, and automatic testing of candidate drugs. Because only limited quantities of candidate drugs are available, testing must be performed on microvolumes (8), for which microfluidics based devices are well suited. By integrating cell treatment steps, a lab-on-a-chip for cellomics may allow the study of the effects of drugs on single living cells and enable fast delivery of drugs to cells (9). Genomic and proteomic analysis have great potential in drug discovery by providing information about the effect of environment, disease, and chemicals upon an organism. While genomics seeks to characterize all of the genes of an organism, proteomics seeks to characterize and identify all proteins expressed within a cell at a given time (10). Devices approaching a lab-on-a-chip for DNA analysis have already been demonstrated (11), however because cell function and biochemical regulation depend on protein activity, among other reasons, interest has shifted to proteomics in drug discovery (12).

Because protein levels vary widely and because there is no protein amplification method comparable to the polymerase chain reaction (PCR) used in genomics, an ideal proteomics method must be highly sensitive. Lab-on-a-chip may be able to offer suitable sensitivity and allow handling of small sample volumes without loss in the processing steps along with greater speed and automation (13,14).

A handheld lab-on-a-chip may provide law enforcement with a mobile laboratory for forensic applications, such as analysis of illegal drugs. Another possibility is a portable detector of explosive residues (15). NASA is considering microfluidics based systems to send to Mars (7). While these are but a sampling of possible applications of lab-on-a-chip currently being explored, upon its realization, it appears this technology will satisfy scientific needs not yet conceived.

Microfluidics

Physicist Richard Feynman noted in his lectures that physical laws do not simply scale down leaving the behavior of matter unchanged (16). He later proposed in his 1959 lecture entitled "There's Plenty of Room at the Bottom" that the extremely small should be utilized, noting that the laws of physics do not prevent vast miniaturization, only that no one had "gotten around to it" (17). While his lecture did not mention it

specifically, microfluidics exemplifies his thoughts about miniaturization. Microfluidics

can be defined as fluid flow in channels of dimension ranging from 1 μm to 1 mm (18).

One of the first examples of a device employing microfluidic flow, considered to

be the first μTAS, was a gas chromatographic air analyzer (19). Preceding the coining

of the term μTAS by Manz et al., this device received little attention possibly because of

the lack of experience in the scientific community (20). Other early research utilizing

microfluidics include IBM's work on the ink jet printer nozzle (21). There are also

several interesting properties useful to biology at this scale (22). First, as mentioned in

the context of lab-on-a-chip, the fluid volumes are dramatically reduced. The surface

area to volume ratio is several orders of magnitude greater than at the macroscale. This

allows more rapid heat transfer, useful in capillary electrophoresis. At the microscale,

surface tension forces become significant, increasing the distance liquids travel due

solely to capillary forces, useful in some pumping systems.

Perhaps the most important difference at the microscale is the dramatic decrease

in the Reynolds number, a unitless number representing the ratio of the inertial forces to

the viscous forces. The Reynolds number is used to determine whether flow will be

laminar or turbulent. If the Reynolds number is less than 2300, which is predominantly

the case in microfluidics, the flow follows a laminar regime. Because of laminar flow,

two streams can flow parallel to one another, mixing only by diffusion. Diffusion is the

process by which particles move from a more concentrated to a less concentrated area,

resulting in a more uniform distribution. This property is useful in some biological

situations, such as diffusion based separation and detection (23). The predictability of

laminar flow also makes it useful in moving packets of fluid in a controlled manner (22).

While the diffusive mixing employed in microfluidics allows for greater control

of mixing processes, diffusion can be a slow process, especially when attempting to mix

large particles (22). One of the most important features of microfluidic based lab-on-a-

chip systems is greater speed than comparable macroscale systems, so methods to

improve microfluidic mixing must be devised. While chaotic, turbulent flow is

frequently used to achieve rapid mixing at the macroscale, it is typically unavailable at

the microscale (24). In order to improve the rate of mixing, much research has gone into

constructing passive and active micromixers (60). Bend-induced vortices can enable a

process called "chaotic advection," which accelerates mixing (25). One group has called

the mixing of macromolecular analytes in times of less than 10-20 seconds the "Achilles

heel" of lab-on-a-chip systems with channel width greater than 50 μm that rely on

diffusive mixing (26).

Design and improvement of mixers and other microfluidic components requires

accurate understanding of flow within microchannels (27). Currently, flow is modeled

using computational fluid dynamics (CFD) software and measured using optical based

flow visualization methods. The most popular of these methods is particle image

velocimetry (PIV) (27,28). In PIV, fluorescently labeled seed particles are placed within

the flow and observed using a microscope and camera. While this method provides high

resolution, the seed particles are small enough to be affected by Brownian motion,

making them move randomly. Because they do not follow the flow exactly, time

averaging is necessary, making PIV unsuited for unsteady flows (29). This system

requires that at least part of the structure under study be optically transparent. Also, the

presence of fluorescently labeled chemicals may interfere with processes being observed

(22).

Magnetic Resonance Imaging

Magnetic resonance imaging (MRI) is a non-invasive imaging method that uses

magnetic fields and radio frequency (RF) pulses to interact with nuclear spins in order to

collect signals. Through a Fourier transform, these signals are converted into images.

The most prominent application of MRI is in clinical diagnosis, where it provides

detailed images of soft tissue without the ionizing radiation of X-ray or computed

tomography (CT). Nuclear magnetic resonance (NMR) spectroscopy is another

application useful in biology, physics, and chemistry. MRI is capable of providing a

multitude of environmental variables about matter, and has an established history of non-

invasively quantifying fluid flow (30).

MR flow measurement techniques have been employed in clinical magnetic

resonance angiography (MRA) to study blood flow, but because of the lack of temporal

resolution of clinical scanners, these images are frequently constructed using a gating

mechanism such that each MR echo occurs at the same point of the cardiac cycle. MRI

is also capable of studying flow in non-clinical settings. However, because of its low

temporal resolution, its usefulness is often limited to slow and steady or pulsate flows.

Faster MR imaging techniques such as echo planar imaging (EPI) have had some

success in imaging faster and more complex turbulent flows by increasing the temporal

resolution of MRI, and new techniques continue to be developed.

Recent advances at the Magnetic Resonance Systems Laboratory (MRSL) at

Texas A&M University have enabled dramatically accelerated image acquisition rates

using a 64-channel array coil. Single Echo Acquisition (SEA) imaging allows for

complete image acquisition with one echo (31), a rate two orders of magnitude faster

than standard scanners. This increased imaging rate allows observation and

quantification of flow phenomena not accessible by conventional MRI systems, such as

fast or turbulent flow.

II. BACKGROUND

Microfluidics

The field of microfluidics has seen tremendous growth due largely to the applications of microfluidic devices in life sciences and due to the availability of microscale manufacturing techniques stemming from the developments of the integrated circuit industry. Microfluidic devices seek to harness the unique physical properties of the microscale, allowing experiments not possible at the macroscale (22).

Construction

Microfluidic devices employ several fabrication techniques including micromachining, soft lithography, in situ construction, and micromolding, each suited to different applications (22). Micromachining methods can be applied to silicon and glass (32), providing a high degree of precision. Silicon and glass are beneficial to chemistry applications by withstanding many temperatures and strong solvents; however silicon is not always desirable in biological applications due to its optical opacity, which prevents use of microscopy. Glass offers optical transparency, but there are fewer micromachining processes available. The highly specialized labor and equipment employed in micromachining results in high costs, making this method less desirable.

Soft lithography overcomes such high costs by offering less specialized fabrication

methods involving molding of Polydimethylsiloxane (PDMS), a two-part polymer. It is

convenient, fast, and is well suited for features of dimension greater than 50 μm,

commonly used in biology (33). In situ construction uses liquid-phase

photopolymerization, lithography, and laminar flow to create microfluidic systems (34).

This method requires little specialized equipment or skills, resulting in lower cost, but it

offers limited device dimensions. Micromolding utilizes injection of heated

thermoplastic polymer materials, facilitating quick and inexpensive creation of a molded

part (22). Both soft lithography and micromolding require use of masters for molding,

which can be created with micromachining.

Physics

The physics of the microscale offer several challenges as well as advantages over

comparable macroscale methods. The Reynolds number (*Re*) is a unitless number used

to classify flow. The flow regime is laminar for Reynolds numbers less than 2300,

turbulent for Reynolds numbers greater than 2300, and at Reynolds numbers near 2300.

Laminar flow is streamline and predictable, while turbulent flow is chaotic. The

Reynolds number is the ratio of the inertial forces to the viscous forces, defined as

$$\mathrm{Re} = \frac{\rho \upsilon D_H}{\mu},$$

where ρ is density, υ is velocity, D_H is hydraulic diameter, and μ is dynamic

viscosity. The hydraulic diameter is four times the cross-sectional area divided by the

wetted perimeter, and is on the order of micrometers in microfluidic systems. Thus, at

microscale dimensions, the Reynolds number is low and flow occurs predominantly in a

laminar regime, meaning that streams flowing in parallel will not turbulently mix as is

common at the macroscale. Laminar flow offers the benefit of controlled movement of a

packet of fluid, useful in cellular analysis (22). An interesting property of fluid with

Reynolds numbers significantly less than 1 is that time makes no difference, allowing

motion to be symmetric and processes to be reversible (35). For instance, a scallop

propels itself by opening its shell slowly to take in water and then closing it quickly to

squirt water. At such low Reynolds numbers inertia has little effect and the scallop

would simply move back and forth, retracing the same path (36).

At the microscale, diffusion becomes more significant and can facilitate mixing.

Because diffusion time varies with the square of the diffusion distance, decreasing

distances to the microscale allows diffusion to take place much more quickly (22,35).

However, diffusion constants for solutions containing macromolecules are high,

resulting in slower diffusion (37). Surface area to volume ratios are large in

microfluidics, allowing rapid heat transfer while at the same time reducing pumping

efficiency. In addition, surface tension forces become more significant at the

microscale, increasing the effects of capillary forces.

Components

Microfluidic devices integrate several key microfluidic components that take

advantage of microscale physics (22). Valves are necessary for control and

manipulation of fluid flow. Both active and passive valves have been developed, where

active valves use energy and passive valves do not. Mixers, discussed later, seek to

overcome the mixing limitations imposed by unavailability of turbulence by increasing

the area over which diffusion occurs. Microscale fluid motion can be generated using

mechanical pumps, or through nonmechanical means (20). Forces can be applied within

a microchannel or at its inlets and outlets (38). Electro-osmotic flow, for example,

causes flow to move relative to stationary charged boundaries, which offers several

advantages such a flat rather than parabolic velocity profile and easy control of flow in

multiple channels (39). Development of these and other components would benefit from

new microfluidic visualization techniques.

Microfluidics Toward Lab-on-a-Chip

Several of the necessary processes for integrating a full laboratory onto a chip are

sample preparation, injection, fluid and particle handling, mixing and chemical reaction,

separation, and detection (40). While only a few examples are mentioned, there are

many microfluidic devices capable of these tasks. Sonication, for instance, is a method

of sample preparation that uses acoustic energy to physically disrupt bacteria spores for

PCR analysis of DNA. This decreases analysis time by removing the need for manual

pre-PCR processing of samples (41). Preparation of nucleic acids for PCR analysis is

also performed using microchip-based solid-phase extraction, which isolates PCR

amplifiable DNA (42). There are many methods of preconcentration of samples, such as

through generation of concentration gradients (43).

Sample injection methods have been utilized for rapid screening for explosives

and nerve agents such that upon their detection, an alarm is triggered and detailed

identification is performed (44). Fluid and particle handling has been accomplished

using electrokinetic control to transport reactants (45). Chemical microreactors have

been constructed, such as one capable of derivatization of amino acids through heating

(46). In derivatization, the original structure of an analyte is converted into another

molecule or mixture of reaction products (47). Separations can be performed at the

microscale using capillary electrophoresis, which has the potential to assay hundreds of

samples in minutes or less (48). Rapid heat transfer due to high surface area to volume

ratios allows higher voltages in capillary electrophoresis, improving separation

performance and analysis speeds (49).

Also crucial to microfluidic systems are microscale sensors, which allow

detection. If a microfluidic system is used to perform an analysis, detection is needed to

retrieve the results. Because of the small volumes, detection systems must be highly

sensitive (22). Several methods include chemiluminescence, electrochemical detection,

fluorescence, and mass spectrometry (40). For instance, a chemical reaction monitored

with chemiluminescence has been used to detect chromium (III) in the presence of

chromium (VI) (50).

Microfluidic Systems

Various microfluidic systems with biological and medical applications have been

developed (22). These integrate multiple microfluidic devices, many approaching or

realizing full labs-on-a-chip. Several systems for macromolecular analysis have been

developed. A system capable of performing PCR amplification and electrophoretic size

separation for DNA analysis (51) integrates reaction and separation steps. Enzyme

assays are performed with microfluidic systems to determine an enzyme's reaction

kinetics, allowing decreased times, decreased reagent consumption, and higher

sensitivity (22). One of the first microscale enzyme assays uesd electrokinetic flow to

control the dilution and mixing of reagents (52). Immunoassays are capable of

exploiting the sensitivity and selectivity of antibody-antigen interactions (53) and have

applications in pharmaceutical research and development (22). Immunoassay

microfluidic systems that integrate mixing, reaction, and separation steps have been

developed (54). DNA hybridization arrays allow the simultaneous study of changes in

the expression of thousands of genes (55).

There are several microfluidic systems for cellular analysis (22). Microfluidic

flow cytometry systems attempt to sort, analyze, and count single cells. Flourescence-

activated cell sorting systems do this by placing cells in lines (14). Use of cell-based

assays for high throughput drug discovery screening has been discussed (56). Cell-

based biosensors use living cells to detect biologically active agents, allowing screening

of an agent's functional activity without knowing its chemistry. This is beneficial to

pharmacology, cell biology, toxicology, and environmental monitoring. Microfluidics

based cellular biosensors allow greater portability by addressing issues such as sample

preparation, maintenance of the biological environment, and integration of electronics

for data collection and analysis (57). Microfluidic cell culturing systems study the

properties of isolated single cells with their environments (58). Experimental culturing

of mouse embryos indicates that a microchannel culture system may more closely match

in vivo environments than traditional *in vitro* culture methods (59).

Microscale Mixing

As discussed above, low Reynolds numbers are a key feature of microfluidics.

Consequently, flow through almost all microscale channels occurs in a laminar regime.

This lack of turbulence means that mixing occurs only due to diffusion, which while

faster at the microscale, remains in many instances inferior to the rapid turbulent mixing

common to the macroscale. Diffusion is not fast enough in some microfluidic settings,

such as those requiring mixing of large particles or cells (22). Rapid mixing is important

in microfluidic systems for biochemistry analysis, drug delivery, and nucleic acid

sequencing or synthesis (60). Immunoassay, DNA hybridization, and cell-molecule

interaction are analyses that require rapid mixing (61). In addition, many biological

processes and lab-on-a-chip systems require mixing of reactants for chemical reactions.

An understanding of micromixers is important to forming a better understanding

microscale transport phenomena (60). Micromixers can be classified as either passive or

active, with passive requiring no external energy and active using external forces.

Passive Micromixers

Because of laminar flow conditions, passive micromixiers operate by diffusion

and chaotic advection. Diffusion based passive micromixers seek to increase the surface

area over which diffusion can occur, allowing the diffusion path to be shortened.

Parallel lamination micromixers separate flow into several smaller streams which are

laterally alternated to increase the boundary surface between them, increasing diffusion

(62). Serial lamination micromixers split and join streams horizontally and next

vertically, achieving multi-level lamination (63). Injection micromixers function by

splitting a solute into streams and injecting them into the solvent (60), which is useful in

sample preparation (64). Chaotic advection is a phenomena in which simple velocity

fields produce chaotic particle trajectories, indicative of elongation and distortion of

material interfaces, which increases diffusion and leads to rapid mixing (37). It can by

achieved by altering the channel shape to split, stretch, fold and break the flow, such as

by insertion of obstacles (60) and can occur in laminar flow regimes (65).

Active Micromixers

Active micromixers function by using external fields to cause mixing, however they are often more complex, more difficult to integrate into systems, and more expensive than passive micromixers (60). Pressure field disturbance can facilitate mixing, such as by using pulsatile flow micropumps (66). Electro-hydrodynamic forces can cause fluids with different electrical properties to mix when placed in an electric field (67). Electrokinetic forces can be used to drive parallel and serial mixing in a T-mixer (45). Mageto hydrodynamic mixers use arrays of electrodes, an electrolyte solution, and a magnetic field to induce Lorentz forces in a fluid, causing complex flow fields (68).

Microscale Flow Visualization

The continued development of microfluidic devices must be met with suitable methods of visualizing microscale fluid flow, such as determination of velocity information. Microfluidic flow visualization is essential for understanding microscale fluid behavior and in analyzing, developing, and evaluating new microfluidic processes (27). Development of medical micro-assay systems also requires understanding of blood flow mechanics at the microscale (69). Flow visualization methods seek to alter the

fluid only enough to detect fluid transport, such that the motion of the fluid is not

affected, that is, the method should be non-invasive. Because this is often impossible,

flow visualization methods must be validated by demonstration that disturbances to the

flow are negligible. Alternatively, methods are validated if it can be shown that despite

introduction of disturbances, the undisturbed flow information can be resolved. Many

macroscale flow visualization techniques, such as the injection of dyes (70), cannot be

employed at the microscale because of their invasiveness (27).

Particle Image Velocimetry

The leading method of microscale flow visualization is particle image

velocimetry (PIV), in which seed particles are placed within flow and optically observed

to obtain velocity information. PIV was first developed at the macroscale, where two-

component velocity information is obtained for a two-dimensional plane by pattern

matching velocimetry (PMV) and particle tracking velocimetry (PTV). PMV commonly

obtains two sequential images at a set time delay using a laser and charge-coupled

device (CCD) camera. Each image is of a small area, and by comparing patterns of the

particles within images, a vector field is obtained for that area. This method enables

instantaneous velocity measurements, but uses averaging for steady flow to improve

accuracy (27). PTV determines the velocity field by tracking individual particles, giving more velocity information per interrogation than PMV, however PTV requires more image acquisitions for reliable particle pairing. PMV and PTV were combined to create so called "super-resolution PIV" (27,71).

Micro-Particle Image Velocimetry (μPIV)

The first microscale resolution particle image velocimetry (μPIV) system used an epifluorescent microscope, 100–300 μm diameter seed particles, and an intensified CCD camera to obtain particle-image fields, yielding spatial resolutions of 6.9 x 6.9 x 1.5 μm (28). This system operates similarly to macroscale PIV, with several differences. The seed particles are much smaller, small enough to exactly follow the flow without blocking channels, yet large enough to allow imaging and to dampen Brownian motion. Polystyrene particles were labeled with fluorescent dye, causing them to absorb blue light at a wavelength of 469 nm and in turn emit green light at a wavelength of 509 nm. The bulk velocity of this setup was 50 μm/s and the time delay between successive images was 68.5 ms. One improvement on this method involves using a pulsed laser to achieve spatial resolutions of 13.6 x 0.9 x 1.8 μm and a 500 ns delay between sequential images (72).

There are several disadvantages inherent in using fluorescent microspheres as seed particles. As this is an optical technique, a fundamental limitation is the need for optical access to the flow, requiring transparent boundaries. Because of the small size of the particles, they are affected by Brownian motion. This causes them to move randomly, initially resulting in error of 9%, which was reduced by ensemble averaging (28). Particles typically fluoresce only on the surface or weakly through the volume due to quenching effects, resulting in lower signal-to-noise ratios (27,73). Also, particles are generally hydrophobic due to polystyrene construction, which can lead to aggregation of particles, nonspecific absorption of hydrophobic solutes on particle surfaces, and adhesion of particles to microchannel walls (73). Problems may arise in using electroosmotic flow because the particles exhibit interfacial phenomena, have electrophoretic motion, and can affect electrokinetic flow and interfacial phenomena at the boundary (73).

Fluorescence

In fluorescence, a photon is absorbed by a fluorosphore, the fluorosphore becomes excited for 1-10 ns, and a photon of a lower energy is emitted (27). Fluorescence intensity fields resulting from mixing a dyed fluid with an undyed fluid

provide concentration fields, allowing assessment of mixing performance (61). Presence

of fluorescently labeled chemicals may also interfere with processes under investigation

(22). When using top-down fluorescence microscopy to assess the degree of mixing,

incomplete mixing along the depth of the channel cannot be experimentally detected

(74). Because of the short fluorescent lifetime, this technique does not allow tagging,

however photobleaching is a process in which fluorospheres are chemically altered by

exposure to excitation light (61). The resulting "tagged" dark area can then be followed,

allowing velocimetry.

Magnetic Resonance Imaging

Imaging

Magnetic resonance imaging (MRI) is based on the interaction of protons in a

strong magnetic field with radio frequency (RF) energy (75). When placed in a strong

magnetic field ($\mathbf{B_0}$), the magnetic moments of protons align with and against the field,

precessing around it. A slight imbalance in the number of protons in each of these states

is present yielding a net magnetization for MR imaging. Exposure to a time varying

radio frequency (RF) magnetic field ($\mathbf{B_1}$) at the resonance frequency causes protons to

shift states. This allows magnetic moments, or "spins," to be tipped 90° such that they

precess in a plane orthogonal to $\mathbf{B_0}$. While the net magnetization has components in this plane (during T1 decay) with coherent phase (during T2 decay), a signal is detectable by an RF coil.

Based on a concept originally proposed by Paul Lauterbur (76), for which he was awarded a Nobel Prize, gradient magnets create spatially dependent variations in $\mathbf{B_0}$, which are used for slice selection and to spatially encode frequency and phase into the spins. Phase encoding requires a repetition of RF pulses and gradient magnets, each with a phase encoding gradient of different magnitude. This set of pulses, called a pulse sequence, has a set repetition time (TR) between RF pulses and echo time (TE) between excitation and received signal. The signals or "echoes" resulting from exposure to an RF pulse are demodulated and sampled, each forming one line of what is called Fourier space, or *k*-space. After data collection, a 2-dimensional inverse Fourier transform is performed on *k*-space, extracting the encoded spatial information to form an image. A gradient echo sequence uses one RF pulse per echo, while a spin-echo sequence employs a second RF "refocusing" pulse. This second pulse causes the precession of the magnetic moments to re-phase, creating a greater signal while at the same time lessening the effects of magnetic field inhomogeneities.

Velocity Measurement

The motion sensitivity of MRI has an established history and has undergone

many developments to form tools for non-invasive blood flow measurement

(30,75,77,78,79). For instance, heart motion has been observed using an MR imaging

method based on tagging (explained below) myocardial tissue with RF saturation before

acquiring images, allowing study of biomechanical properties of normal and abnormal

heart muscle (80). In an improvement on this method, higher resolution spatial patterns

of altered magnetization have been used to assess motion of the heart (81). Non-clinical

flow velocity studies can also benefit from the non-invasiveness of MRI. Measurements

of flow through a step stenosis were performed to assess the limitations of MRI

velocimetry in complex geometries (82). Both spin tagging, a time-of-flight effect, and

phase contrast measurements were compared to computational fluid dynamics results.

Spin-tagging operates by selectively tagging spins and observing them a fixed

time later to assess motion. This is done by saturating spins prior to imaging so that they

yield no signal during subsequent echoes until they have undergone T1 decay. Selective

saturation can be used to insert a grid of lines, which appear black in the images due to a

lack of signal. This has been accomplished using a DANTE pulse train (83) and a sinc-

modulated pulse train (84). Velocity information is obtained by dividing the

displacement of a grid square by time between images. Spin-tagging can provide a

qualitative picture of two-components of complex motion within a slice, but the

resolution of quantitative velocity information is limited by size of the grid squares

(82,85).

Phase contrast methods are based on flowing fluid acquiring a different amount

of phase than its stationary surroundings. This can be accomplished using a bipolar

gradient pulse, which has no effect on stationary spins but causes moving spins to

acquire phase, where the amount of phase acquired is dependent on the velocity of the

fluid. Single component velocity information for each pixel can be acquired for flow

through a slice.

Complex Flow Studies

While MRI is commonly used in flow studies, many of these rely on steady or

periodic flow due to the limitations in temporal resolution of conventional MR imaging.

For instance, in clinical MR angiography, a gating mechanism can ensure that echoes

occur at the same point of the cardiac cycle. Alternative MR imaging methods have

been used to image complex unsteady flow phenomena, such as turbulence. Several of

these methods have been reviewed. Echo planar imaging (EPI) (86) has been used to accelerate image acquisition by employing time dependent magnetic field gradients to acquire multiple lines of k-space in one excitation.

The structure of a turbulent puff has been imaged using a one-shot imaging technique based on echo-planar imaging. These puffs occur in flow with a transitional Reynolds number when a disturbance is introduced at the pipe inlet. Images of turbulent puffs in flow of Reynolds numbers 2000 and 2250 were acquired in 20.48 ms, with 150 ms between consecutive images (87). An echo-planar approach has also been applied to acquire "instantaneous" velocity measurements of a turbulent puff across a two-dimensional plane (88). This approach is limited by the time difference between spin echoes, which becomes significant for unsteady flows. Data acquisition time was 48 ms and velocity measurements are acquired at different times, meaning that measurements are not truly instantaneous. EPI has been used to image the distribution of local shearing motion in circular pipes (89), yielding agreement with theory at the downstream region of a turbulent puff. Image acquisition time was 20.48 ms and consecutive images were taken 200 ms apart. Spatial tagging with EPI has also been used to image turbulent

motion (85), allowing visualization of complex motions by a single image. Image

acquisition time was 21.12 ms and consecutive images were taken 200 ms apart.

EPI has been used to study the dependence of the NMR signal from turbulent

flow on velocity (90). Images of 64 x 64 resolution were acquired with a TE of 28 ms.

Total acquisition time per image was 33 ms and the sequence was repeated every 250

ms. This allowed acquisition of 32 consecutive images in 8 s. *Re* was varied from 0 to

6270. Inspection of the images shows increasing complexity with increasing *Re*.

Individual vortices and eddies can be seen, and their movement is visible when images

are viewed as movies. The degree of turbulence was quantified by calculating the

standard deviation of each pixel. The amount of shear present was related to the signal

amplitude, and the mean cross-stream velocity was related to the phase.

More recently, an EPI based imaging sequence called the gradient echo rapid

velocity and acceleration imaging sequence (GERVAIS) has been used to acquire three

velocity components from a single excitation over a timescale of 60 ms (91). Image

resolution of 64 x 32 was obtained. This was used to study laminar and turbulent flow,

with *Re* up to 5000. The velocity fluctuations are shown to be small compared to local

velocities, establishing that the acquisition times are short enough that the images are

effectively instantaneous. As *Re* was increased, qualitative observation showed loss of radial symmetry and parabolic velocity profiles, turbulent eddies, and high shear at the walls.

Single Echo Acquisition Magnetic Resonance Imaging

SEA MRI drastically reduces image acquisition time by eliminating phase encoding using a 64-element array of planar pair coils (31). The concept of using multiple receive coils to decrease acquisition time has been demonstrated before, such as in sensitivity encoding (SENSE), which is based on the encoding effect of receiver sensitivity (92). Using RF coils with highly localized field sensitivity patterns, SEA performs spatial localization by combining conventional frequency encoding along the axis of the array elements with the spatial information provided by each element. A one-dimensional FFT is performed on the echo from each coil, spatially resolving the encoded frequencies and providing one line of the image (93).

Using a gradient echo sequence modified to eliminate phase encoding, a TE of 3 ms and a TR of 5 ms have been achieved, allowing imaging at 200 frames per second (94). These MR "snapshots" allow visualization of dynamic processes, such as motion, which cause artifacts in conventional MRI. The parallel array is 13 cm by 8.1 cm, with

the 64 parallel elements along the 13cm length. This gives the array a resolution of 2

mm along the array encoding direction and 1 mm along the frequency encoding

direction.

Microscale Magnetic Resonance

As discussed earlier, detection is critical in retrieving results from a µTAS.

Nuclear magnetic resonance (NMR) spectroscopy, therefore, has been integrated into a

microfluidic system to perform analysis on the output of a chip-based capillary

electrophoresis device (95). This system incorporates a planar RF detector coil for

NMR, however its sensitivity was not adequate for detection of concentrations typical of

the output of capillary electrophoresis. Another system was developed using multiple

solenoidal microcoils (96), which have higher sensitivity. This approach splits the flow

from a separation capillary into multiple outlets and stops one segment of it to obtain

high resolution NMR spectra while flow continues through the other segment. Research

continues into development of planar microcoils because they can be built using

processes based on photolithography and predictions indicate that performance may

approach that of solenoid microcoils (97).

While these methods focus on detection, MRI velocimetry has also been performed in microchannel networks (J. Georgiadis, personal communication). Conventional MR phase-contrast velocimetry was performed using a standard flow-compensated spin-echo sequence with bipolar gradients. Imaging was performed in a 7.6 cm inner diameter RF coil with an acquisition time of 12 min 51 s for each of two velocity components. This system yielded high resolution (~ 100 μm^2 pixel size) velocity images for *Re* of order 1.

III. METHODS

Conventional MR Flow Imaging

It is important first to establish the limitations of conventional MR flow imaging before demonstrating the advantages of SEA flow imaging. A flow phantom, a device for assessing the performance of an MRI system, was constructed (Fig. 1) with 3/16" (0.476 cm) and 5/16" (0.794 cm) inner diameter tubing connected in series to provide two flow velocities, each traversing both directions along the main magnetic field. The tubing passed through a 3" (7.62 cm) inner diameter PVC pipe cylinder containing copper sulfate doped water. This solution yields a strong uniform background signal, making the flow information easily visible, while also lessening magnetic field inhomogeneities near the imaged fluid. Copper sulfate solution was pumped through the tubing by a Cole-Parmer variable flow rate peristaltic pulsating pump.
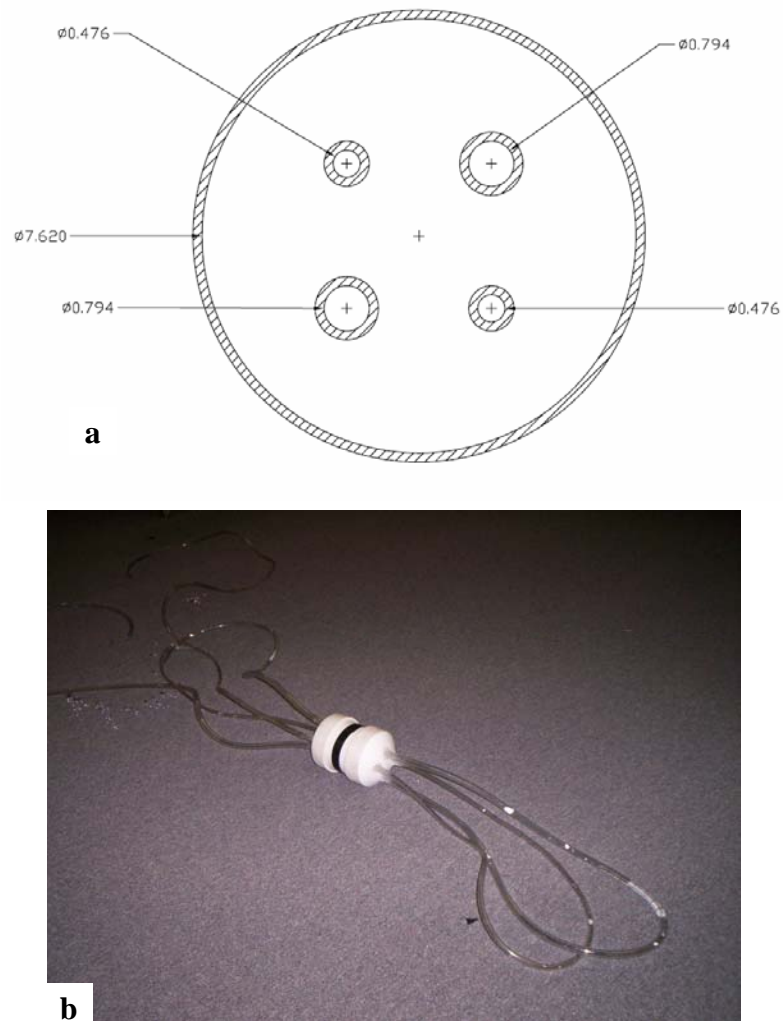
FIG. 1. Cylindrical phantom. (a) Cross section sketch (cm). (b) Photograph.

Imaging of this phantom was performed with a 4.7 Tesla/33 cm Bruker/GE

Omega MRI system using a lab-built birdcage radio frequency coil. Spin-echo imaging

was performed with a TE of 15 ms and a TR of 300 ms. Gradient echo imaging was also

performed and the pulse sequence was configured for a TE of 28 ms and a TR of 300

ms. Images were acquired at pump settings of 2, 4, and 6, which resulted in the flow

velocities indicated in Table 1. At resolutions of 128x256, scan time was 38 seconds.

The *k*-space data was imported into MATLAB and a 2-dimensional Fourier transform

was performed, yielding magnitude and phase images.

Table 1

Flow in cylindrical phantom

Pump Setting	Volumetric flow rate (mL/sec)	3/16" tubing average velocity (cm/s)	5/16" tubing average velocity (cm/s)
2	7	39	14
4	13	73	26
6	20	112	40

SEA Flow Imaging

A separation channel phantom (Fig. 2), modeled after a microfluidic device

studied by the Lab for Quantitative Visualization in Energetics at the University of

Illinois at Urbana-Champaign (UIUC) (J. Georgiadis, personal communication), was

constructed for analysis with SEA imaging. Because the MRSL operates a printed

circuit board (PCB) prototyper, the phantom was constructed of several layers of PCB.

The boards were precisely cut using the prototyper and copper surfaces were removed

using PCB etching solution. Four layers of PCB were glued together with epoxy to form

the phantom, and a thin sheet of plastic served as a boundary between the fluid and the parallel array. The signal to noise ratio decreases rapidly with distance from the array, so this layer must be as thin as possible.

Fluid enters and exits from the sides, where two 3/16" (0.476 cm) inner diameter tubes terminate. These tubes then bend 90 degrees to leave the magnet. The limited bending radius allowed by the tubes resulted in making the phantom smaller. Water flows into the phantom, strikes a rectangular obstruction, separates, travels around the obstruction, and recombines to exit. The same pump as before was operated at settings of 0.5, 1, and 2, resulting in the flow velocities in Table 2.
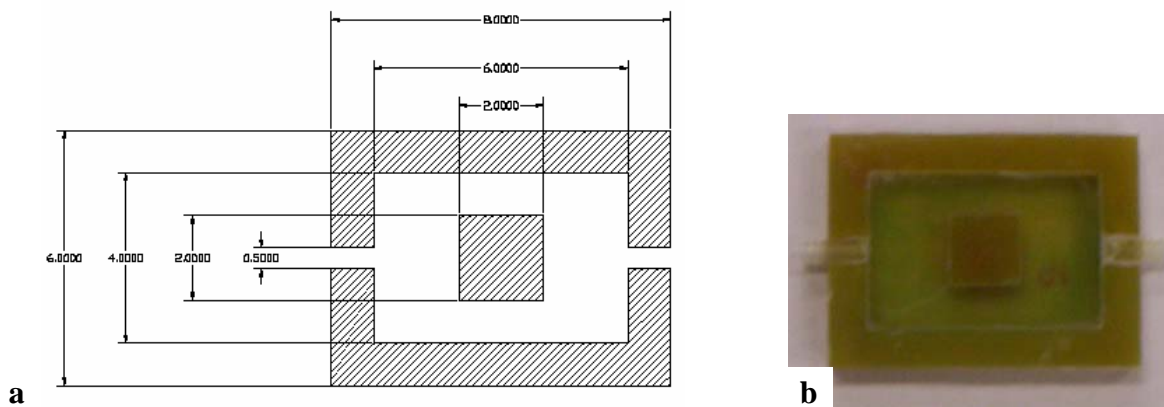
FIG. 2. First separation channel phantom. (a) Sketch (cm). (b) Photograph.

Table 2

Flow in first separation channel

Pump setting	Volumetric flow rate (mL/sec)	Average velocity entering phantom (cm/s)	Average velocity while separated (cm/s)
0.5	1.5	8.4	3
1	3	16.8	6
2	7.7	43.2	15.4

A second separation channel phantom (98) (Fig. 3) has been constructed using the same methods as the first, only with more robust X-ray film as the boundary between the fluid and the parallel array. This design incorporates ducts so that the fluid enters and exits from a different side than the previous phantom. Moving the fluid entry ports proved key to expanding the phantom to cover more of the parallel array while still allowing room for termination of the tubing. The larger size enables better matching of the phantom to capabilities of SEA. Also, this phantom more strictly adheres to the proportions of the device studied by UIUC.
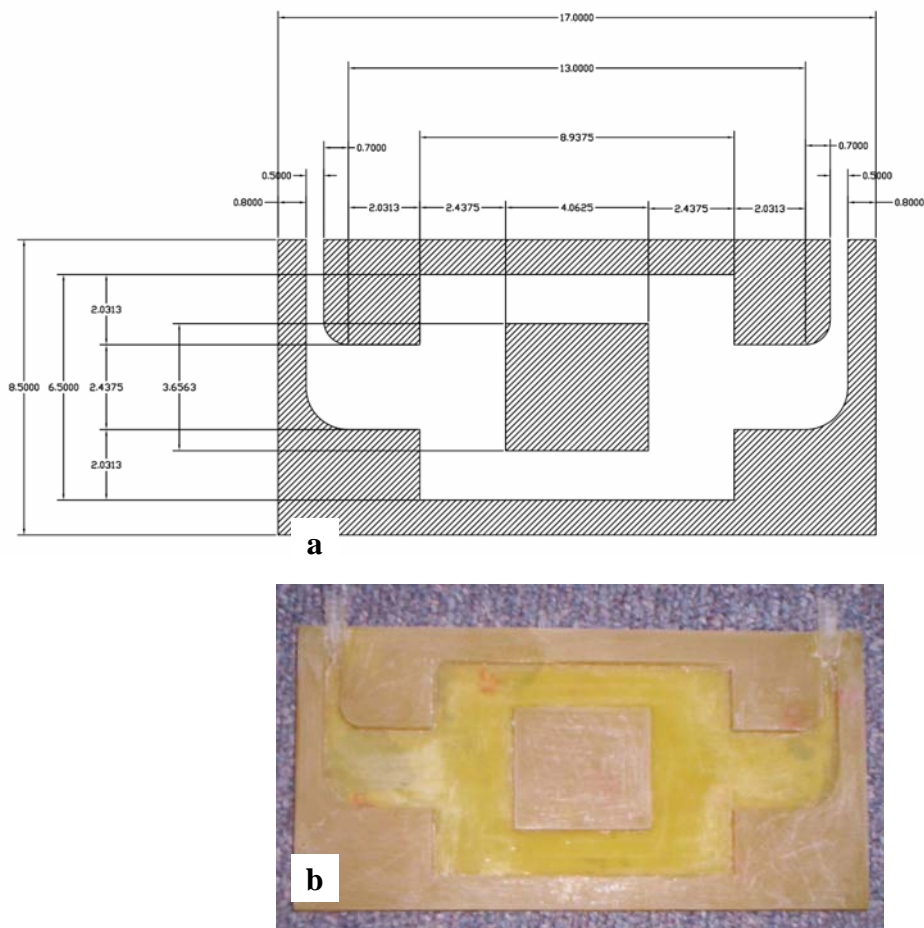
FIG. 3. Second separation channel phantom. (a) Sketch (cm). (b) Photograph.

Table 3 indicates the flow velocities at different locations within the phantom at

various pump settings. These velocities are averaged over the cross sectional area of the

channels and also time averaged over the pulses of the pump. Table 4 indicates

Reynolds numbers in the second separation channel. Because the flow does not have

adequate distance to fully develop into a laminar or turbulent regime, these values

cannot indicate with complete accuracy the flow regime in any part of the phantom.

They are based on a rectangular channel and do not take into account the effects of the

obstruction. However, these values give a general order-of-magnitude idea of what

regime might be expected.

Table 3

Flow in second separation channel (98)

Pump Setting	Volumetric flowrate (mL/sec)	Average velocity 3/16" tubing (cm/s)	Average velocity entry/exit (cm/s)	Average velocity separated (cm/s)
0	0	0	0	0
1	3.0	17.0	2.5	2.1
2	7.7	43.2	6.3	5.4
3	12.5	70.2	10.2	8.8
4	15.6	87.7	12.8	11.0
5	20	112.3	16.4	14.1

Table 4

Reynolds numbers in second separation channel

Pump Setting	Volumetric flow rate (mL/sec)	Re 3/16" tubing	Re entry/exit	Re separated
1	3.0	910	232	177
2	7.7	2310	588	450
3	12.5	3753	955	731
4	15.6	4691	1194	914
5	20.0	6005	1528	1170

The same MR system described above was used, with a parallel plate RF volume

coil and a 64-element array of planar pair coils. The first separation phantom was

imaged using both conventional and SEA modes, while the second was imaged with

SEA only. In conventional imaging, the volume coil was used for transmit and receive,

TE was 20 ms and TR was 250 ms. SEA imaging was performed using the volume coil

for transmission, the array for receive, and a conventional non-refocused gradient echo

pulse sequence with a phase compensation gradient pulse rather than a phase encoding

table (98). This sequence was modified to include spin-tagging based on DANTE pulses

(Fig. 4), which saturate grids of spins for subsequent tracking.
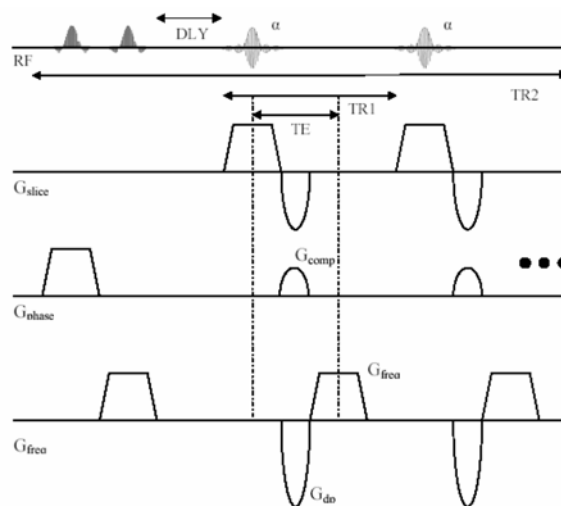
FIG. 4. Spin-tagging sequence. Uses 2-dimensional DANTE pulse train preceding a
recalled gradient echo sequence. (98)

Initially, only vertical tag lines were saturated, then a diagonal grid of tag lines was employed. Application of the spin-tags took 14 ms. The first separation channel was imaged at 40 fps, while the second separation channel was imaged at 200 fps. The 200 fps pulse sequence had a TE of 3 ms and a TR of 5 ms. Distilled water flowed through the phantom rather than copper sulfate solution in order to increase the T1 relaxation time, allowing the spin-tags to remain longer. However, this is at the cost of weaker signals. Fig. 5 illustrates how each phantom rests on the parallel array.
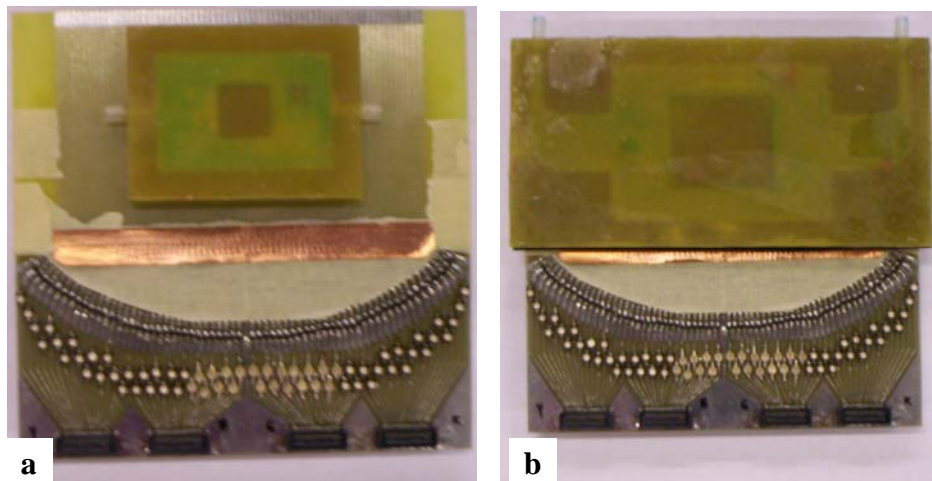
FIG. 5. Separation phantoms on array. (a) First separation channel. (b) Second separation channel.

IV. RESULTS

Conventional MR flow imaging shows limits

Conventional MR spin-echo magnitude images illustrate flow artifacts. Fig. 6 is

of volumetric flow rates of 7, 13, and 20 mL/sec (see Table 1). The four circles are the

tubes in which flow is occurring, the larger two are the 5/16" (0.794 cm) tubing and the

smaller the 3/16" (0.476 cm) tubing. In all images, the flow direction is perpendicular to

the imaged slice and the velocity is fastest in the smaller tubes, causing artifacts to

present there first. As the flow rate is increased, time of flight artifacts appear as

complete signal void (black) in the areas of high velocity, such as in all but one tube in

Fig. 4c. Phase artifacts present as distortion above and below the flow area along the
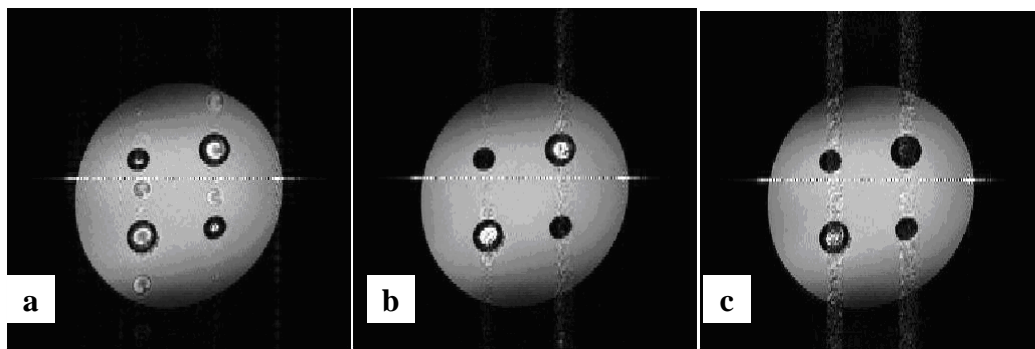
phase encoding direction.

FIG. 6. Conventional MR magnitude images of cylindrical phantom. (a) 7 mL/s. (b)
13 mL/s. (c) 20 mL/s.

Spin-echo phase images (Fig. 7) show wrapped flow information due to excess

flow sensitization, indicating a non-uniform velocity profile, consistent with pressure

driven flow. Looking at the tubes in each image, the wrapping is indicated by the

number of alternations of black and white, which increases with velocity.
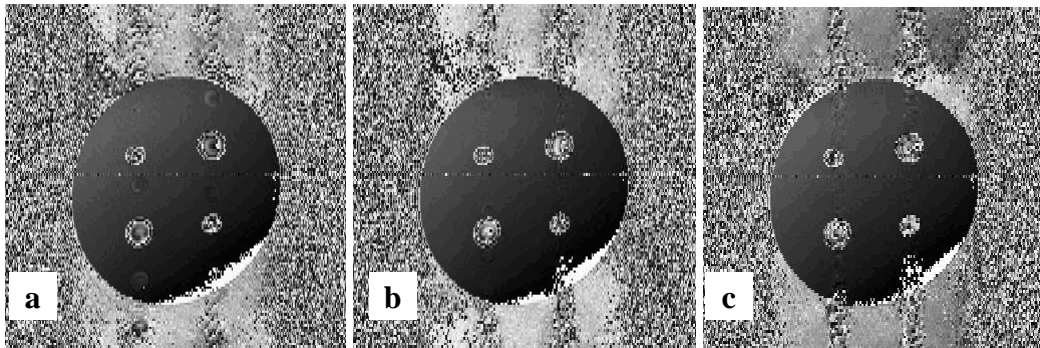

FIG. 7. Phase maps of cylindrical phantom. (a) 7 mL/s. (b) 13 mL/s. (c) 20 mL/s.

The gradient echo sequence with a short echo time has less sensitization,

decreasing the amount of phase wrapping. Figs. 8a, 8b, and 8c illustrate flow rates of 0,

7 and 13 mL/sec, respectively. The time of flight signal void artifact as well as the

ghosting phase artifacts are less pronounced in the resulting magnitude images.
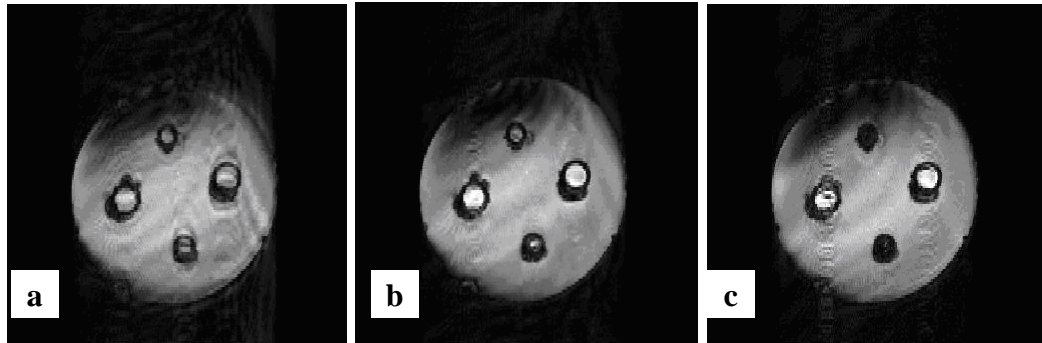
FIG. 8. Gradient echo magnitude images of cylindrical phantom. (a) 0 mL/s. (b) 7 mL/s. (c) 13 mL/s.

The shorter gradient echo time decreased the wrapping in the phase images (Fig. 9), however the inhomogeneities of the magnetic field were more pronounced, making velocity information difficult to extract. Qualitative information can be obtained by comparing the brightness within the tubes to that of the surrounding area. With no flow (Fig. 9a), both sets of tubes show no contrast with the surrounding area. At 7 mL/sec (Fig. 9b), the offset begins to present, indicating flow. The lowest tube is beginning to show wrapping, indicating that velocity is exceeding measurement capabilities. At 13mL/sec (Fig. 9c), all of the tubes show some degree of wrapping.
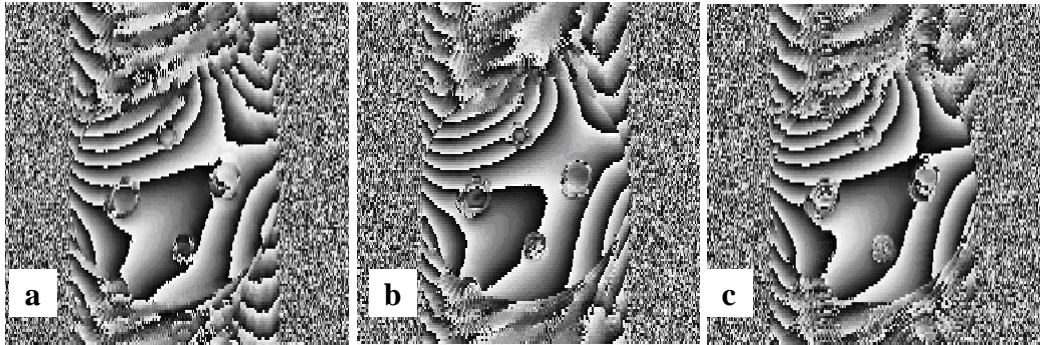
FIG. 9. Gradient echo phase images of first phantom. (a) 0 mL/s. (b) 7 mL/s. (c) 13 mL/s.

Advantages of SEA are clear

Conventional spin-echo images of the first separation channel phantom (Fig. 10) again demonstrate limitations in temporal resolution. Velocities are listed in Table 2. Fig. 10a shows stationary flow with no tags, Fig. 10b shows flow at a pump setting of 0.5 with spin tags and 4 averages. Artifacts begin to present in the areas of fastest flow, where the fluid strikes the obstruction from below. Figs. 10c and 10d indicate pump settings of 1 and 2, respectively, with 16 averages. Artifacts intensify in Fig. 10c and the complete loss of signal in Fig. 10d is because fluid leaves the imaged slice before it can experience both 90 degree and 180 degree RF pulses.
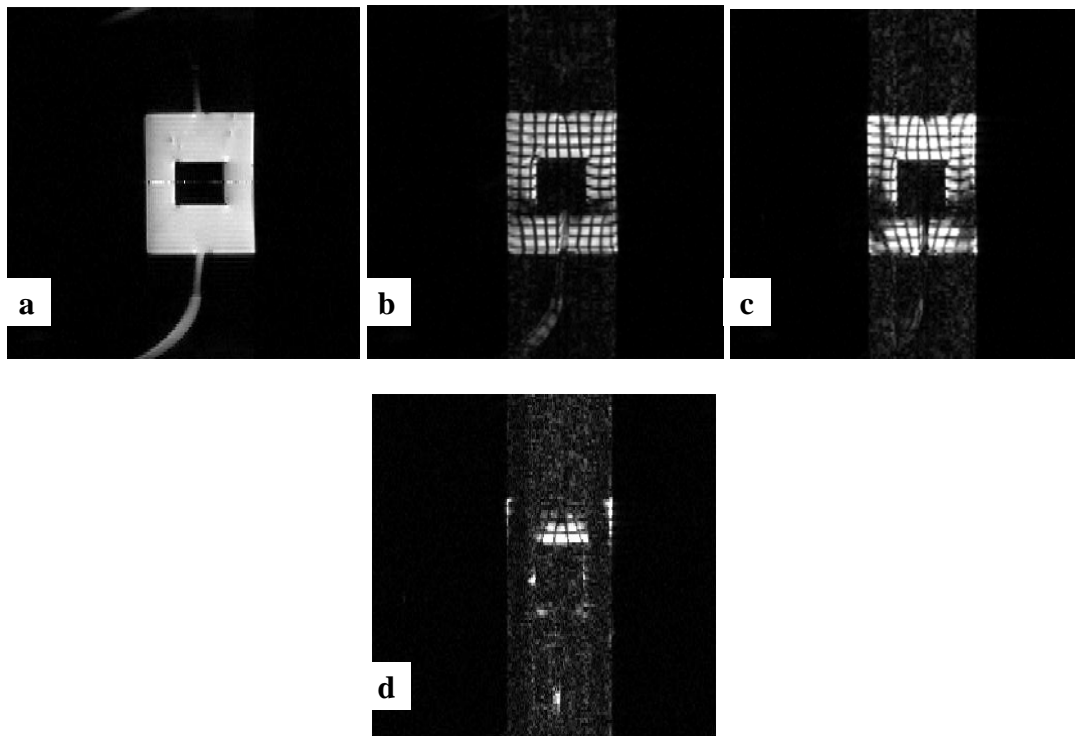
FIG. 10. Conventional images of first separation channel. (a) Stationary with no tags.
Images with tags at (b) 1.5 mL/s, (c) 3 mL/s, (d) 7.7 mL/s.

SEA images of the first separation channel (Fig. 11) are of limited resolution due

to the small size of the phantom relative to the resolution of SEA, however, qualitative

information is available. The time between acquisitions of each of the following images

was 25 ms, for an image acquisition rate of 40 frames per second. The images in Fig. 11

were taken at a flow rate between that of 10b and 10c, however no such artifacts present

in the SEA images. Fig. 11a was acquired immediately after tagging, 11b was 50 ms

after tagging, and 11c was 100 ms after tagging. Flow enters at the top and exits at the

bottom. When viewed in rapid succession as a movie, rotation is visible in the upper

half of the phantom, and the tag lines in the bottom move toward the center as fluid from

each half of the phantom recombines. At the same time, the tag lines fade as time passes
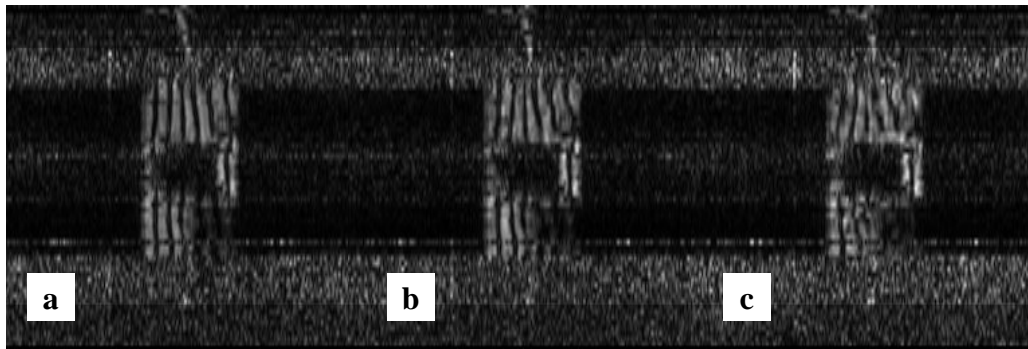
due to T1 decay of the spin tags.

FIG. 11. SEA images of first separation channel. (a) 1st frame. (b) 2nd frame.
(c) 4th frame.

As the second separation channel spans more of the array, the tag lines are more

visible. Fig. 12 shows vertical tag line images at a pump setting of 2.75, while the pump

setting for Fig. 13 is 4.5. Corresponding velocities may be interpolated from Table 3.

These images were captured from a movie, with each frame separated by 5 ms.

Observation of the tag line motion along the lowest horizontal boundary of the images

yields the velocity at which the fluids flow parallel to the boundary as the two halves

recombine. At a pump setting of 2.75 (Fig. 12), the tag lines at the boundary move at 11

cm/s, and at a pump setting of 4.5 (Fig. 13), this velocity is 13.7 cm/s. Rotation is

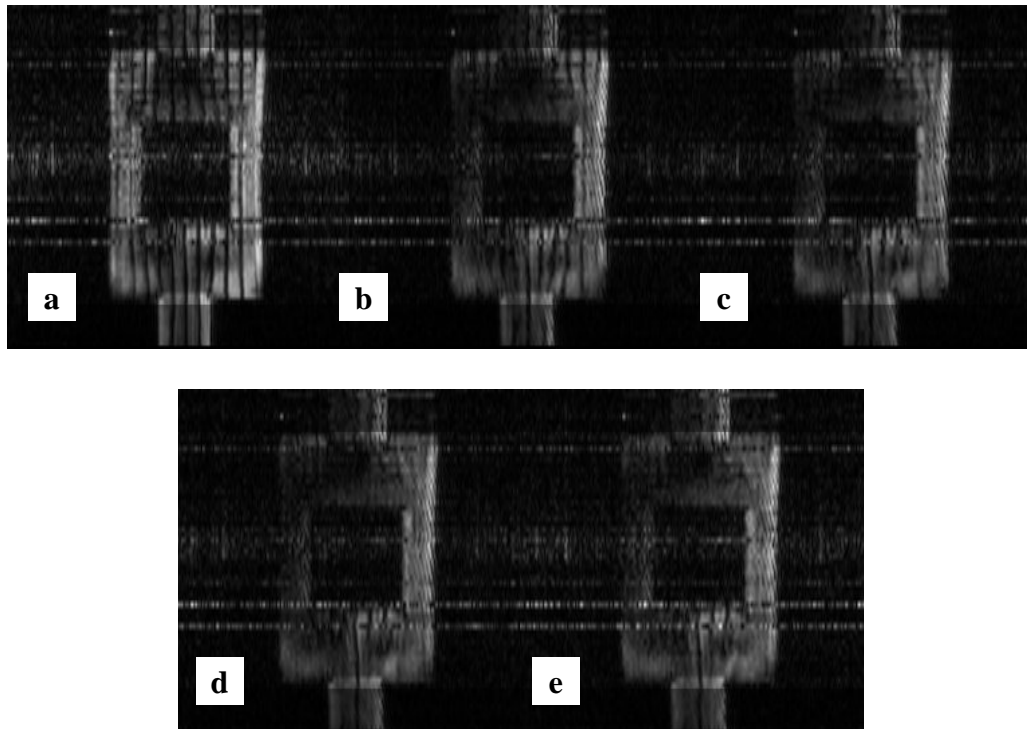visible in the upper right corner, indicative of turbulence.

FIG. 12. SEA vertical tag line images of second separation channel at a pump setting of 2.75. (a) 1st frame. (b) 5th frame. (c) 10th frame. (d) 15th frame. (e) 20th frame.
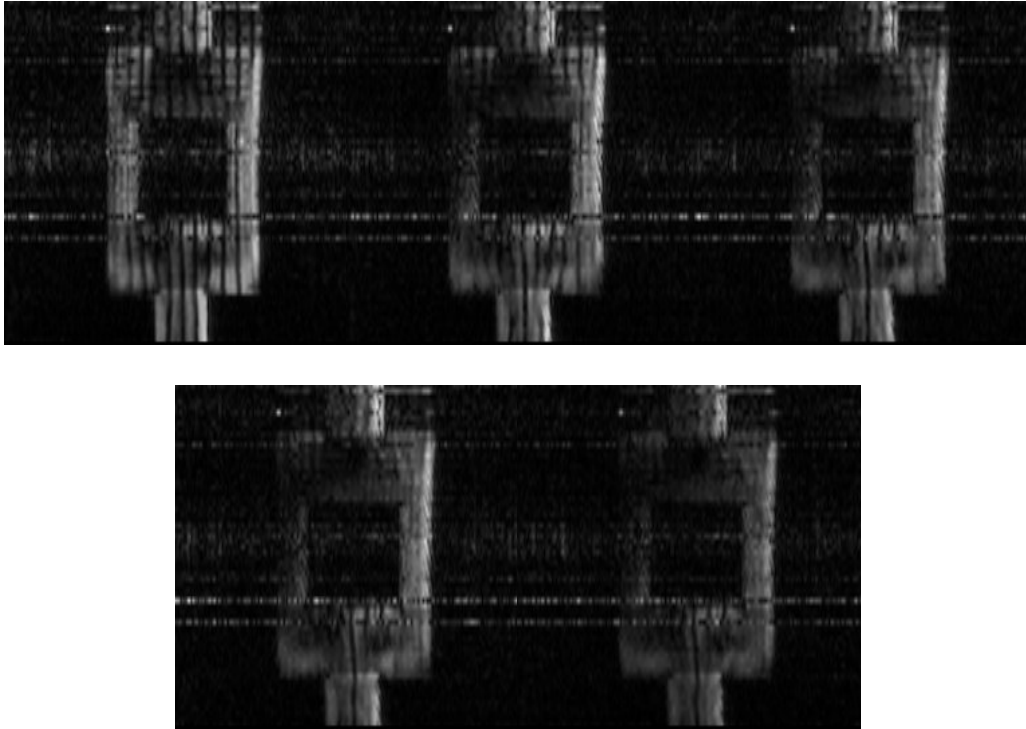
FIG. 13. SEA vertical tag line images of second separation channel at a pump setting of 4.5. (a) 1st frame. (b) 5th frame. (c) 10th frame. (d) 15th frame. (e) 20th frame.

The SEA images of the second separation channel in Figs. 14 and 15 (98) have

diagonally oriented tag lines. The lines are 2 mm wide and are separated by 6 mm. This

allows better visualization of motion with the resolution of the 64-channel array coil,

which is lower in the array encoded direction. The position of the phantom on the array

in relation to the images is indicated in Fig. 16. Each row in Figs. 14 and 15 represents

an increasing pump setting (Table 3), starting at 0. For each pump setting, 64 images

were acquired, followed by a 3 second delay to allow T1 decay. During this delay, the

pump setting was increased by 1 unit. The first column of Figs. 14 and 15 represents the 1st frames, the second column represents the 10th frames, and the third column represents the 20th frames. Thus, the images in the first column were taken immediately after the tagging, those in the 2nd column were taken 50 ms after the tagging, and those in the 3rd column were taken 100 ms after the tagging.

While viewing the images as animations provides the best visualization of the fluid dynamics, the isolated frames in Figs. 14 and 15 can provide some details (98). Row 2, with a pump setting of 1, shows that the flow travels on the left side of the entry port, which can be expected due to the bend shown in Fig. 16. At higher flow rates, an area of stationary fluid can be seen above the obstruction, as the fluid travels around that area to exit the phantom. In the animations, eddies are visible in the lower left corner. Complex flow can also be seen as the fluid recombines to exit the phantom. Quantitative velocity information can also be extracted. By comparing the images in the 1st and 20th frame in row two, the fastest flow in the inlet channel moves 1 cm, meaning that its bulk velocity is 10 cm/s.

FIG. 14. SEA diagonal tag line images of second separation channel (Pump settings 0 through 2). Each row corresponds to a pump setting indicated in Table 3. The 1st, 2nd, and 3rd columns are the 1st, 10th and 20th frames acquired following the application of spin-tags. (98)
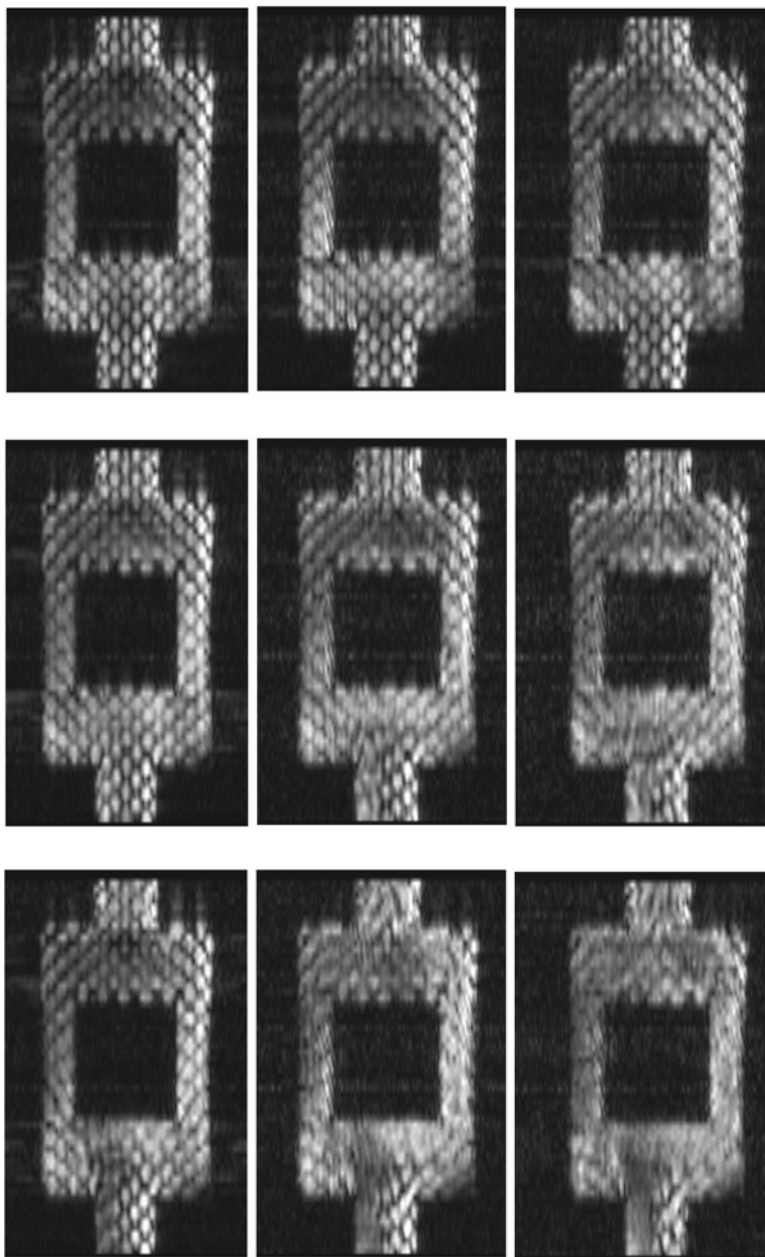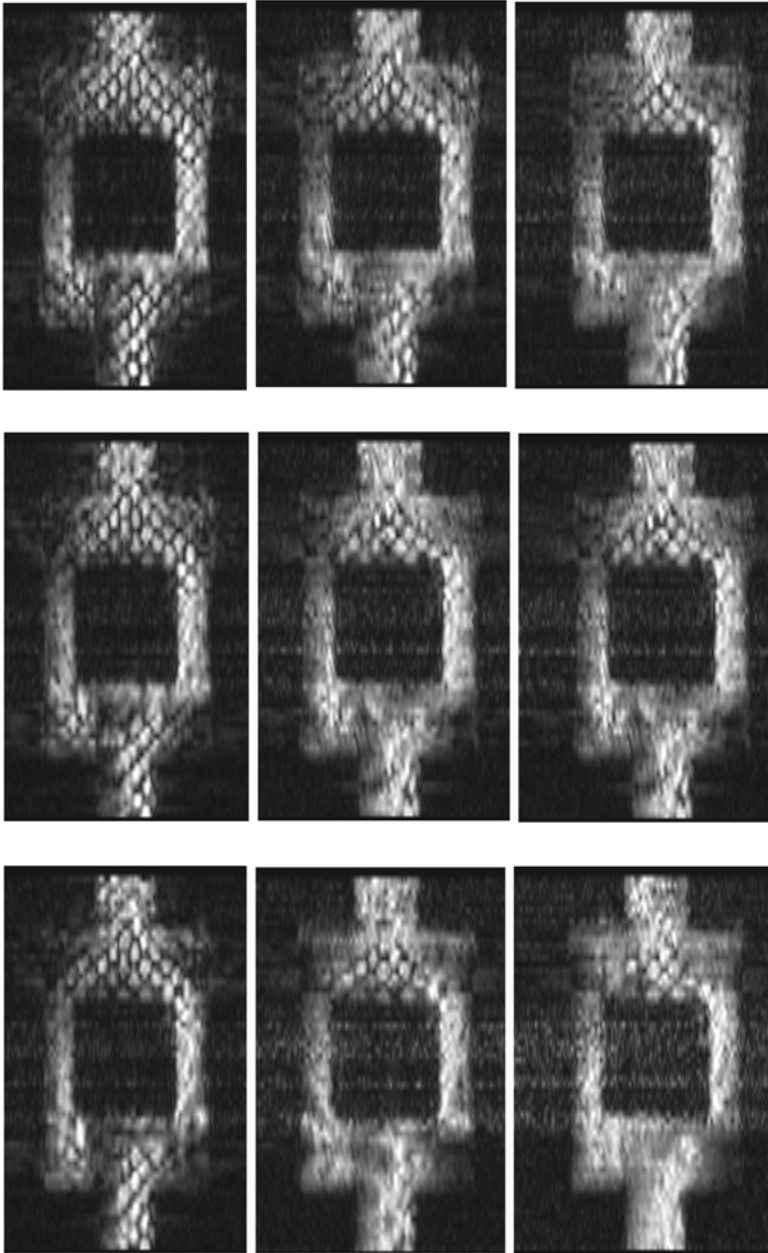
FIG. 15. SEA diagonal tag line images of second separation channel (Pump settings 3 through 5). Each row corresponds to a pump setting indicated in Table 3. The 1st, 2nd, and 3rd columns are the 1st, 10th and 20th frames acquired following the application of spin-tags. (98)
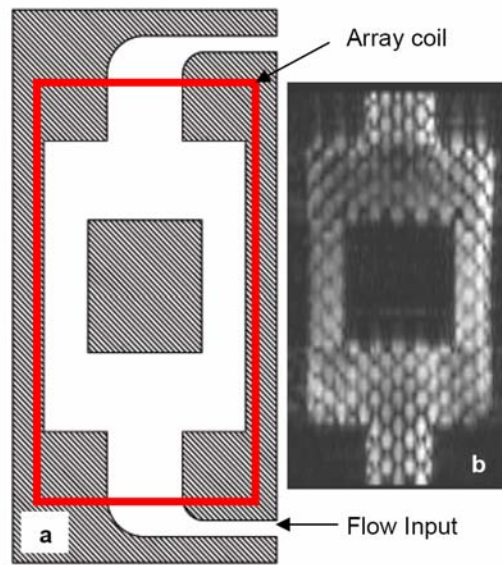
FIG. 16. Second separation channel orientation. (a) Sketch, including termination ducts. The box indicates the array coil. (b) MR image of stationary flow for comparison. (98)

V. DISCUSSION

SEA imaging couples the non-invasiveness of MRI that is relied upon daily in the clinical setting with real-time visualization capability. By demonstrating the ability to view complex flow phenomena inaccessible to conventional MRI, SEA is shown to hold promise as a tool for quantifying flow. Building on the research seeking to integrate NMR spectroscopy in microfluidic devices, RF microcoils could also be integrated in microfluidic devices in a parallel array configuration. This would enable SEA imaging and thus provide a noninvasive method of visualizing microfluidic flow at high temporal resolution without requiring optically transparent boundaries.

The capability of visualizing complex flow phenomena, such as turbulence and mixing, could prove key in refinement and development of new microfluidic devices. Although turbulence is unavailable at the microscale, other complex flows are, such as chaotic advection utilized in micromixers. Improved microscale flow visualization techniques will aid in the development of microfluidic devices, furthering novel biological technologies such as lab-on-a-chip. Such technologies are posed to usher in a new age of medical discovery and treatment.

REFERENCES

1. Figeys D, Pinto D. Lab-on-a-chip: a revolution in biological and medical sciences. Anal Chem 2000;72A:330–335.

2. Manz A, Graber N, Widmer HM. Miniaturized total chemical analysis systems: a novel concept for chemical sensing. Sens Actuators B 1990;B1:244–248.

3. Tudos AJ, Besselink GAJ, Schasfoorte RBM. Trends in miniaturized total analysis systems for point-of-care testing in clinical chemistry. Lab Chip 2001;1:83–95.

4. Kricka LJ. Microchips, microarrays, biochips and nanochips: personal laboratories for the 21st century. Clin Chim Acta 2001;207:219–223.

5. McGlennen RC. Miniaturization technologies for molecular diagnostics. Clin Chem 2001;47:393–402.

6. Hudson MP, Christenson RH, Newby LK, Kaplan AL, Ohman EM. Cardiac markers: point of care testing. Clin Chim Acta 1999;284:223–237.

7. Service RF. Coming soon: the pocket DNA sequencer. Science 1998;282:399–401.

8. Kricka LJ. Miniaturization of analytical systems. Clin Chem 1998;44:2008–2014.

9. Andersson H, van den Berg A. Microfluidic devices for cellomics: a review. Sens Actuartors B 2003;92:315–325.

10. Sanders GHW, Manz A. Chip-based microsystems for genomic and proteomic analysis. Trends Anal Chem 2000;19:364–378.

11. Burns, et.al. An integrated nanoliter DNA analysis device. Science 1998;282:484–487.

12. Burbaum J, Tobal GM. Proteomics in drug discovery. Curr Opin in Chem Biol 2002;6:427–433.

13. Mouradian S. Lab-on-a-chip: applications in proteomics. Curr Opin in Chem Biol 2001;6:51–56.

14. Lee SJ, Lee SY. Micro total analysis system (μ-TAS) in biotechnology. Appl Microbiol Biotechnol 2004;64:289–299.

15. Verpoorte E. Microfluidic chips for clinical and forensic analysis. Electrophoresis 2002;23:677–712.

16. Feynman RP. The character of physical law. Cambridge, MA: MIT Press;1967. p 96.

17. Feynman RP. There's plenty of room at the bottom. J Microelectromechan Syst 1992;1:60–66.

18. Sharp KV, Adrian RJ, Santiago JG, Molho JI. Liquid flows in microchannels. In: Gad-el-Hak M (ed) The MEMS handbook. CRC, Boca Raton, FL, 2002.

19. Terry SC, Jerman JH, Angell JB. A gas chromatographic air analyzer fabricated on a silicon wafer. IEEE Trans Electron Devices 1979;ED-26:1880–1886.

20. Reyes, DR, Iossifidis D, Auroux P-A, Manz A. Micro total analysis systems. 1. Intorduction, theory, and technology. Anal Chem 2002;74:2623–2636.

21. Bassous E, Taub HH, Kuhn L. Ink jet printing nozzle arrays etched in silicon. Appl Phys Lett 1977;31:135–137.

22. Beebe DJ, Mensing GA, Walker GM. Physics and applications of microfluidics in biology. Annu Rev Biomed Eng 2002;4:261–286.

23. Weigl BH, Yager P. Microfluidic diffusion-based separation and detection. Science 1999;283:346–347.

24. Beebe DJ, Trumbull JD, Glasgow IK. Microfluidics and bioanalysis systems: issues and examples. Proc 20 Annu Int Conf IEEE Eng in Med and Biol Soc 1998;20:1692–1697.

25. Yi M, Bau HH. The kinematics of bend-induced mixing in micro-conduits. Int J Heat Fluid Flow 2003;24:645–656.

26. He B, Burke BJ, Zhang X, Zhang R, Regnier FE. A picoliter-volume mixer for microfluidic analytical systems. Anal Chem 2001;73:1942–1947.

27. Sinton D. Microscale flow visualization. Microfluid Nanofluid 2004;1:2–21.

28. Santiago JG, Wereley ST, Meinhart CD, Beebe DJ, Adrian RJ. A particle image velocimetry system for microfluidics. Exp Fluids 1998;25:316–319.

29. Sato Y, Irisawa G, Ishizuka M, Hishida K, Maeda M. Visualization of convective mixing in microchannel by fluorescence imaging. Meas Sci Technol 2003;14:114–121.

30. Fukushima E. Nuclear Magnetic Resonance as a Tool to Study Flow. Annu Rev Fluid Mech 1999;31:95–123.

31. McDougall MP, Wright SM. 64-Channel Array Coil for Single Echo Acquisition Magnetic Resonance Imaging. Magnetic Resonance in Medicine 2005;54:386–392.

32. Voldman J, Gray ML, Schmidt MA. Microfabrication in biology and medicine. Annu Rev Biomed Eng 1999;10:401–425.

33. Whitesides GM, Ostuni E, Takayama S, Jiang XY, Ingber DE. Soft lithography in biology and biochemistry. Annu Rev Biomed Eng 2001;3:335–373.

34. Beebe DJ, Moore JS, Yu Q, Liu RH, Kraft ML, Jo B-H, Devadoss C. Microfluidic tectonics: A comprehensive construction platform for microfluidic systems. Proc Natl Aca Sci U S A 2000;97:13488–93.

35. Brody JP, Yager P, Goldstein RE, Austin RH. Biotechnology at low Reynolds numbers. Biophys J 1996;71:3430–3441.

36. Purcell EM. Life at low Reynolds number. Am J Phys. 1977;45:3–11.

37. Liu RH, Stremler MA, Sharp KV, Olsen MG, Santiago JG, Adrian RJ, Aref H, Beebe DJ. Passive mixing in a three-dimensional serpentine microchannel. J Microelectromech Syst 2000;9:190–197.

38. Stone HA, Stroock AD, Ajdari A. Engineering flows in small devices: Microfluidics toward a lab-on-a-chip. Annu Rev Fluid Mech 2004;36:381–411.

39. Kopp MU, Crabtree HJ, Manz A. Developments in technology and applications of microsystems. Curr Opin Chem Biol 1997;1:410–419.

40. Auroux P-A, Iossifidis D, Reyes DR, Manz A. Micro total analysis systems. 2. Analytical standard operations and applications. Anal Chem 2002;74:2637–2652.

41. Belgrader P, Okuzumi M, Pourahmadi F, Borkholder DA, Northrup MA. A microfluidic cartridge to prepare spores for PCR analysis. Biosens Bioelectron 2000;14:849–852.

42. Wolfe KA, Breadmore MC, Ferrance JP, Power ME, Conroy JF, Norris PM, Landers JP. Toward a microchip-based solid-phase extraction method for isolation of nucleic acids. Electrophoresis 2002;23:727–733.

43. Jeon NL, Dertinger SKW, Chiu DT, Choi IS, Stroock AD, Whitesides GM. Generation of solution and surface gradients using microfluidic systems. Langmuir 2000;16:8311–8316.

44. Wang J, Pumera M, Chatrathi MP, Escarpa A, Musameh M. Single-channel microchip for fast screening and detailed identification of nitroaromatic explosives or organophosphate nerve agents. Anal Chem 2002;74:1187–1191.

45. Jacobson SC, McKnight TE, Ramsey JM. Microfluidic devices for electrokinetically driven parallel and serial mixing. Anal Chem 1999;71:4455–4459.

46. Eijkel JCT, Prak A, Cowen S, Craston DH, Manz A. Micromachined heated chemical reactor for pre-column derivatisation. J Chromatogr A 1998;815:265–271.

47. Krull IS, Deyl Z, Lingeman H. General strategies and selection of derivatization reactions for liquid chromatography and capillary electrophoresis. J Chromatogr B 1994;659:1–17.

48. Dolník V, Liu S, Jovanovich S. Capillary electrophoresis on microchip. Electrophoresis 2000;21:41–54.

49. Manz A, Harrison DJ, Verpoorte EMJ, Fettinger JC, Paulus A, Lüdi H, Widmer HM. Planar chips technology for miniaturization and integration of separation techniques into monitoring systems. J Chromatogr 1992;593:253–258.

50. Xu Y, Bessoth FG, Eijkel JCT, Manz A. On-line monitoring of chromium(III) using a fast micromachined mixer/reactor and chemiluminescence detection. Analyst 2000;125:677–683.

51. Waters LC, Jacobson SC, Kroutchinina N, Khandurina J, Foote RS, Ramsey JM. Microchip device for cell lysis, multiplex PCR amplification, and electrophoretic sizing. Anal Chem 1998;80:158–162.

52. Hadd AG, Raymond DE, Halliwell JW, Jackbson SC, Ramsey JM. Microchip device for performing enzyme assays. Anal Chem 1997;69:3407–3412.

53. Colyer CL, Tang T, Chiem N, Harrison DJ. Clinical potential of microchip capillary electrophoresis systems. Electrophoresis 1997;18:1733–1741.

54. Cheng SB, Skiller CD, Taylor J, Attiya S, Lee WE. Development of a multichannel microfluidic analysis system employing affinity capillary electrophoresis for immunoassay. Anal Chem 2001;73:1472–1479.

55. Freeman WM, Robertson DJ, Vrana KE. Fundamentals of DNA hybridization arrays for gene expression analysis. Biotechniques 2000;29:1042–1055.

56. Sundberg SA. High-throughput and ultra-high-throughput screening: solution- and cell-based approaches. Curr Opin Anal Biotechnol 2000;11:47–53.

57. DeBusschere BD, Kovacs GTA. Portable cell-based biosensor system using integrated CMOS cell-cartridges. Biosens Bioelectron 2001;16:543–556.

58. Inoue I, Wakamoto Y, Moriguchi H, Okano K, Yasuda K. On-chip culture system for observation of isolated individual cells. Lab Chip 2001;1:50–55.

59. Raty S, Walters EM, Davis J, Zeringue H, Beebe DJ, Rodriguez-Zas SL, Wheeler MB. Embryonic development in the mouse is enhanced via microchannel culture. Lab Chip 2004;4:186–190.

60. Nguyen N-T, Wu Z. Micromixers—a review. J Micromech Microeng 2005;15:R1–R6.

61. Oddy MH, Santiago JG, Mikkelsen JC. Electrokinetic instability micromixing. Anal Chem 2001;73:5822–5832.

62. Koch M, Chatelain D, Evans AGR, Brunnschweiler A. Two simple micromixers based on silicon. J Micromech Microeng 1998;8:123–126.

63. Gray BL, Jaeggi D, Mourlas NJ, van Drieënhuizen, Williams KR. Novel interconnection technologies for integrated microfluidic systems. Sens Actuators A 1999;77:57–65.

64. Voldman J, Gray ML, Schmidt MA. An integrated liquid mixer/valve. J Microelectromechan Syst 2000;9:295–302.

65. Jones SW, Thomas OM, Aref H. Chaotic advection by laminar flow in a twisted pipe. J Fluid Mech 1989;209:335–357.

66. Deshmukh AA, Liepmann D, Pisano AP. Continuous micromixer with pulsatile micropumps. In: Proceedings of the IEEE Solid-state Sensor and Actuator Workshop, Hilton Head Island, SC, 2000. 73 p.

67. El Moctar AO, Aubry N, Batton J. Electro-hydrodynamic micro-fluidic mixer. Lab Chip 2003;3:273–280.

68. Bau HH, Zhong J, Yi M. A minute magneto hydro dynamic (MHD) mixer. Sens Actuators B 2001;79:207–215.

69. Chang W, Trebotich D, Lee LP, Liepmann D. Blood flow in simple microchannels. In: Proceeding of the first annual international IEEE-EMBS special topic conference on microtechnologies in medicine and Biology, Lyon, France, 2000. p 311.

70. Reynolds O. An experimental investigation of the circumstances which determine whether the motion of water shall be direct or sinuous, and of the law of resistance in parallel channels. Phil Trans R Soc Lond 1883;174:935–982.

71. Keane RD, Adrian RJ, Zhang Y. Super-resolution particle image velocimetry. Meas Sci Technol 6;1995:754–768.

72. Meinhart CD, Wereley ST, Santiago JG. PIV measurements of a microchannel flow. Exp Fluids 1999;27:414–419.

73. Singh AK, Cummings EB, Throckmorton DJ. Fluorescent liposome flow markers for microscale particle-image velocimetry. Anal Chem 2001;73:1057–1061.

74. Johnson TJ, Ross D, Locascio LE. Rapid microfluidic mixing. Anal Chem 2002;74:45–51.

75. Webb A. Introduction to Biomedical Imaging. Hoboken, NJ: John Wiley & Sons; 2003. p 157.

76. Lauterbur PC. Image formation by induced local interactions: Examples employing nuclear magnetic resonance. Nature 1973;242:190–191.

77. Morse, O. C. and Singer, J. R. Blood velocity measurements in intact subjects. Science 1970;170:440–441.

78. Crooks E, Mills CM, Davis PL, Brant-Zawadzki M, Hoenninger J, Arakawa M, Watts J, Kaufman L. Visualization of cerebral and vascular abnormalities by NMR imaging. The effects of imaging parameters on contrast. Radiology 1982;144:843–852.

79. Axel L. Blood flow effects in magnetic resonance imaging. Am J Roentgenol 1984;143:1157–1166.

80. Zerhouni E, Parish DM, Rogers WJ, Yang A, Shapiro EP. Human heart: Tagging with MR imaging—A method for noninvasive assessment of myocardial motion. Radiology 1988;169:59–63.

81. Axel L, Dougherty L. MR imaging of motion with spatial modulation of magnetization. Radiology 1989;171:841–845.

82. Moser KW, Kutter EC, Georgiadis JG, Buckius RO, Morris HD, Torczynski JR. Velocity measurements of flow through a step stenosis using magnetic resonance imaging. Exp Fluids 2000;29:438–447.

83. Mosher TJ, Smith MB. A DANTE tagging sequence for evaluation of translational sample motion. Magn Reson Med 1990;15:334–339.

84. Wu EX, Towe CW, Tang H. MRI cardiac tagging using a sinc-modulated RF pulse train. Magn Reson Med 2002;48:389–393.

85. Kose K. Visualization of turbulent motion using echo-planar imaging with a spatial tagging sequence. J Magn Reson 1992;98:599–603.

86. Mansfield P. Multi-planar image formation using NMR spin echoes. J Phys C: Solid State Phys 1977;10:L55–L58.

87. Kose K. NMR imaging of turbulent structure in a transitional pipe flow. J Phys D: Appl Phys 1990;23:981–983.

88. Kose K. One-shot velocity mapping using multiple spin-echo EPI and its application to turbulent flow. J Magn Reson 1991;92:631–635.

89. Kose K. Visualization of local shearing motion in turbulent fluids using echo-planar imaging. J Magn Reson 1992;96:596–603.

90. Gattenby JC, Gore JC. Echo-planar-imaging studies of turbulent flow. J Magn Reson 1996;121:193–200.

91. Sederman AJ, Mantle MD, Buckley C, Gladden LF. MRI technique for measurement of velocity vectors, acceleration, and autocorrelation functions in turbulent flow. J Magn Reson 2004;166:182–189.

92. Pruessmann KP, Weiger M, Scheidegger MB, Boesiger P. SENSE: Sensitivity encoding for fast MRI. Magn Reson Med 1999;42:952–962.

93. Wright SM, McDougall MP, Brown DG. Single echo acquisition of MR images using RF coil arrays. In: Proceedings of the 2nd Joint EMBS/BMES Conference, Houston, 2002. p 1181.

94. Wright SM, McDougall M, Yallapragada N. Rapid flow imaging using single echo acquisition MRI. ISMRM 13th Scientific Meeting, Miami Beach, FL, 2005.

95. Trumbull JD, Glasgow IK, Beebe DJ, Magin RL. Integrating microfabricated fluidic systems and NMR spectroscopy. IEEE Trans Biomed Eng 2000;47:3–7.

96. Wolters AM, Jayawickrama DA, Webb AG, Sweedler JV. NMR detection with multiple solenoidal microcoils for continuous-flow capillary electrophoresis. Anal Chem 2002;74:5550–5555.

97. Massin C, Vincent F, Homsy A, Ehrmann K, Boero G, Beese P-A, Daridon A, Verpoorte E, de Rooij NF, Popovic RS. Planar microcoil-based microfluidic NMR probes. J Magn Reson 2003;164:242–255.

98. Wright SM, McDougall MP, Bosshard JC. Progress in visualizing turbulent flow using single-echo acquisition imaging. IEEE Eng Med Biol Conf., New York NY, Sept 2006, Submitted.

CURRICULUM VITA

JOHN CARL BOSSHARD

503 Cherry St. #210	jboss@tamu.edu	901 Delaware Dr.
College Station, TX 77840		Temple, TX 76504
Cellular: (254) 760-7093		Home: (254) 770-0111

EDUCATION

Texas A&M University	B.S., Electrical Engineering
College Station, Texas	Minor: Mathematics
Expected Graduation: May 2006	GPA: 3.943/4.0

RESEARCH

Texas A&M University Undergraduate Research Fellows Program Class of 2006

- Thesis: *Applications of MRI in Fluidics*
- Work with Magnetic Resonance Systems Laboratory in exploring new applications of Ultra-fast MRI
- Experience in MR imaging, MR angiography, network analyzer operation
- Constructed flow phantoms

LEADERSHIP EXPERIENCE

Tau Beta Pi, Texas Delta Chapter, Texas A&M University

- President (Spring 2006)
- Vice President (Fall 2005)
- Service Co-chair (Spring 2005)

HONORS AND AWARDS

- Mechanics Scholar
- Dwight Look College of Engineering – Dean's Honor Roll
- Engineering Scholars Program

- Awarded Willard P. Worley '43 Electrical Engineering Scholarship
- Undergraduate Research Awards Program Recipient